Journal of Materials Chemistry B

Accepted Manuscript

ROYAL SOCIETY OF CHEMISTRY

www.rsc.org/materialsB

A mechano-responsive topology provides a highly active yet autogenous surface for erythrocyte lysis towards microfluidic haematology platforms.

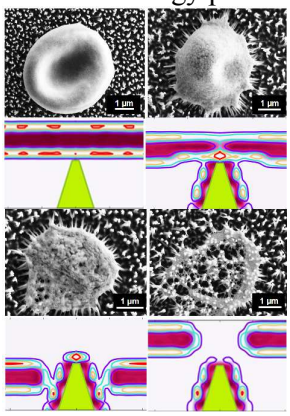

Journal of Materials Chemistry B RSCPublishing

ARTICLE

Nanotopography as a trigger for the microscale, autogenous and passive lysis of erythrocytes

Cite this: DOI: 10.1039/x0xx00000x

Received 00th January 2014,
Accepted 00th January 2014

DOI: 10.1039/x0xx00000x

www.rsc.org/

Vy T. H. Pham,[a] Vi Khanh Truong,[a] David E. Mainwaring,[a] Yachong Guo,[b] Vladimir A. Baulin,[b] Mohammad Al Kobaisi,[a] Gediminas Gervinskas,[c] Saulius Juodkazis,[c,d] Wendy R. Zeng,[a] Pauline P. Doran,[a] Russell J. Crawford,[a] Elena P. Ivanova*[a]

Microscale devices are increasingly being developed for diagnostic analysis although conventional lysis as an initial step presents limitations due to scale or complexity. Here, we detail the physical response of erythrocytes to surface nanoarchitecture of black Si (bSi) and foreshadow its potential in microanalysis. The physical interaction brought about by the spatial convergence of the two topologies: (a) the nanopillar array present on the bSi and (b) the erythrocyte cytoskeleton present on the red blood cells (RBC), provides spontaneous stress-induced cell deformation, rupture and passive lysis within an elapsed time from immobilisation to rupture of ~3 min. and without external chemical or mechanical intervention. The mechano-responsive bSi surface provides highly active yet autogenous RBC lysis and a prospect as a front-end platform technology in evolving micro-fluidic platforms for cellular analyses.

1. Introduction

Microscale devices are increasingly being developed for diagnostic analysis applications, with a view to lowering the cost, analysis time, sample and reagent volumes and decreasing the likelihood of cross-contamination.[1-3] Such microfluidic devices principally focus on two approaches, the active separation of components through the application of external force fields, and the passive separation of components that occur through the hydrodynamic forces that naturally exist within the device.[4-6]

Lim and colleagues[7] have reviewed the applications of cellular biomechanics in terms of probing the mechanical response of diseased cells, physical cell separation based on physical cell properties, and cellular behaviour under imposed shear stresses.[4, 8, 9] It was noted that diseases such as sickle-cell anaemia and malaria reduce the deformability of erythrocytes, which may impact on their transport within the microcirculatory system. Currently, erythrocytes lysis is accomplished by the application of osmotic or pressure stresses (including ultrasonication) to the erythrocyte outer membrane, where pressures can reach 30 kPa before complete lysis occurs,[10, 11] specific chemical treatments,[12, 13] and imposed high electrical fields.[11] Conventional bulk sample preparation techniques that involve cell lysis as a preparative step are increasingly becoming inconsistent with those used in microfluidic devices due to their smaller scale and/or complexity.

Natural and synthetic nanostructured materials that possess topological features with high aspect ratios frequently display unique properties with potential biomedical applications.[14-16] For example, the wing surfaces of the *Psaltoda claripennis* cicada have shown both superhydrophobicity and bactericidal activity against Gram-negative bacteria, where significant physical deformation occurred upon surface contact, which resulted in the physical rupture of the bacterial cells.[17, 18] It was also reported that the nanopillar surface arrays present on *Diplacodes bipunctata* dragonfly wings, together with their synthetic analogue black Si (bSi), exhibited broad bactericidal activity against not only Gram-negative bacteria, but also against the more rigid and lysis resistant Gram-positive bacteria and their spores.[19] The integrity of the cells that came into contact with these surfaces appeared to be significantly disrupted by the nanopillar arrays, indicating that they had been subjected to clear deformation stresses and were subsequently engulfed into the surface.

Cell lysis represents an important haematology platform in diagnostic processes and in monitoring conditions including intracellular haemoglobin, DNA and RNA.[10, 20] Red blood cell lysis, in particular, provides intracellular access to antigens and

parasitized erythrocytes.[21, 22] The macromolecular architecture and micromechanical behaviour of erythrocytes affords them the ability to withstand the deformation that arises from any environmental stresses to which they are exposed within the microcirculatory system.[23] It is, therefore, of considerable interest to investigate the micromechanical behaviour of erythrocytes at the interface between high aspect ratio biomaterials and cells to enable the evaluation of the applicability of such materials in the construction of microfluidic devices. This work has been inspired by several factors; the first is the extensive bactericidal activity that is displayed by the nanoarrays present on the surface of bSi,[19] which takes place as a result of a purely physical interaction between the surface and cells, resulting in cell deformation and death. The second is that bSi surfaces are able to be readily fabricated. It was found that the physical interaction brought about by the spatial convergence of the nanopillar array present on the bSi and the erythrocyte cytoskeleton present on the RBCs resulted in the spontaneous and passive lysis of the cells without the need for additional external chemical or mechanical intervention. This study aims to systematically characterise the nanoscale biointerface in terms of a mechanism for the autogenous rupture of cells, and explore its potential for incorporation within an integrated microfluidic diagnostic device.

2. Experimental details

2.1 Preparation of bSi

The bSi was prepared using a p-type boron doped, 100 mm diameter Si wafer, with specific resistivity of 10 – 20 Ω cm^{-1}, a (100) oriented surface and thickness of 525 ± 25 (Atecom Ltd, Taiwan) substrate. The substrate samples were subjected to reactive ion etching (RIE) using SF_6 and O_2 over a 5 minute period to produce the bSi using an Oxford PlasmaLab 100 ICP380 instrument (Oxford Instruments, Concord, MA, USA). RIE processing was performed in mixed mode, with etching and passivation occurring simultaneously under the following conditions: SF_6 gas flow rate of 65 standard cm^3 min^{-1} (sccm), O_2 gas flow rate of 44 sccm, a pressure of 35 mTorr, 100 W RIE power, electrode temperature of 20 °C and a 10 Torr helium backside cooling pressure.[19] The surface reflection over changed almost linearly from 10 to 20% over the visible spectral wavelength range 400 nm – 800 nm.

2.2 Preparation of erythrocytes

Blood from healthy rats was obtained from the Animal House, Monash University (Animal Ethics Approval MARP/2011/076). Fresh blood was collected in 3.8% (w/v) sodium citrate. The anticoagulated blood was then centrifuged (1400 rpm, 5 min) at 25 °C to separate the blood plasma, buffy coat and to remove the anticoagulant reagent. The separated erythrocytes were then washed twice in phosphate saline buffer (PBS, pH 7.4) and used within 6 hours.

2.3 Scanning electron microscopy

Cells at a density of 4 × 10^6 cells/mL in phosphate buffered saline (PBS) were incubated on the bSi samples in a 12 well culturing plate (Corning® Costar®, Corning, NY, U.S.A.) for 5, 15, 30, 60, 120 and 180 minutes at 37°C. The erythrocytes were also simultaneously incubated on the surface of three control samples, glass cover slips, gelatin (0.1%, Sigma) covered glass and silicon wafers, and examined to confirm the physiological status of the cells after incubation. If the cells retained their biconcave shape, they were considered viable.

After incubation, all samples were washed with 10 mM PBS and fixed in 2.5% glutaraldehyde (Sigma) for 15 min, gently washed with 5 mL of 10 mM PBS, then progressively dehydrated using series of ethanol solutions (30, 50, 70, 90 and 100% v/v). SEM images of the bSi substrates, together with the control surfaces with attached erythrocytes, were examined using a ZEISS SUPRA 40VP field-emission scanning electron microscope (Carl Zeiss NTS GmbH, Oberkochen, BW, Germany) at 3 kV under magnification levels up to 35,000×, as described elsewhere.[17, 24, 25] Images at 1000× magnification was used to quantify the number of attached and ruptured cells on each of the substrates. Ten areas were then selected for analysis from two samples over three independent experiments.

Quantitative topographical analysis of the SEM images was carried out using ImageJ software (NIH USA Image ver. 1.61). Initially, SEM images were band pass filtered to delineate the boundaries of the nanopillar tips and pillar clusters of the uppermost plane that were involved in making initial RBC contact with the bSi. This allowed the pillar tip characteristics and spatial arrangements to be determined. Fast Fourier Transform (FFT) images of top-view SEM images allowed the respective radial distributions to be obtained.

2.4 Confocal laser scanning microscopy

Visualisation of erythrocytes attached to the substrate samples was performed using confocal laser scanning microscopy. Cells at a density of 4 × 10^6 cells mL^{-1} were stained using 1,1'-dioctadecyl-3,3,3',3'-tetramethylindocarbocyanine perchlorate (DiI; Molecular Probes, Eugene, OR, U.S.A.)[26, 27] and incubated with the bSi or silicon wafer substrates in µ-Disc glass-bottom 35 mm culture discs (ibidi GmbH, Martinsried, Germany) for 30 min. The bSi surfaces, with attached erythrocytes, were then washed with PBS, fixed in 4% *p*-formaldehyde and imaged using a FluoviewFV10i inverted microscope (Olympus, Tokyo, Japan).

2.5 Raman spectroscopy

The bSi surface was analysed and the extent of erythrocyte attachment was measured using a Raman micro-spectrometer (WiTEC, Ulm, Germany) with a laser wavelength of 532 nm ($h\upsilon$ = 2.33 eV). A 100× magnification objective (numerical aperture = 1.0) was used to characterise the nanopillars of the bSi, whilst a water-immersion 60× objective lens magnification (numerical aperture = 0.9) was used to map the attachment of

erythrocytes present on the surface of the bSi. A grid of 100 spectra × 100 spectra was acquired for a scanning area of 20 µm × 20 µm. The integration time for a single spectrum was 0.15 seconds. Scanning was independently performed in duplicate using five different samples.

2.6 Modelling

The interaction of the nanopillars with the unanchored RBC membrane was modelled using the Single Chain Mean Field (SCMF) theory, which provides a description of the mechanical and equilibrium properties of lipid bilayers.[28] The probabilities of individual molecule conformations are determined from mean fields as averages over conformations with their probabilities.[29] Lipid molecules are modelled at a coarse-grained level as three freely joined spherical beads of radius 0.4 nm (1 hydrophilic and 2 hydrophobic) connected by a 1 nm stiff bond and interacting through square well potentials. Nanopillars are represented as truncated cones with tip and bottom radii of 0.5 nm and 2.0 nm, respectively. Lipid tails were found to interact strongly with the nanopillars, with an interaction potential of -10 kT when closer than 0.8 nm.

3.1 Characterisation of bSi nanoarrayed surfaces

The SEM images (Fig. 1a) of the bSi produced by RIE for 5 minutes display a disordered array of hierarchical structures arising from clustering of pillar tips (scale bar 500 nm). The subsequent image analysis demonstrated that the area population distribution of the nanopillar system (Fig. 1b) reached a maximum when the pillars were in the range between approximately 49 nm to 100 nm in diameter, the latter representing the magnitude of the nanopillar tip clusters (dimers, trimers). Fast Fourier Transform analysis of the SEM images resulted in images that exhibited an intense ring extending to four broad orthogonal lobes from this secondary structure, from which a grey scale intensity profile analysis allowed an average frequency distance between adjacent nanopillars of 185 nm to be determined (Fig. 1c, d) and without preferential orientation. A typical side view SEM image, generated by prior fracturing (Fig. 1e, f), highlighted a characteristic protrusion shape that exhibited widths between approximately 38 nm and 72 nm and lengths of approximately 616 nm, as diagrammatically represented in Fig. 1(f).

3. Results and discussion

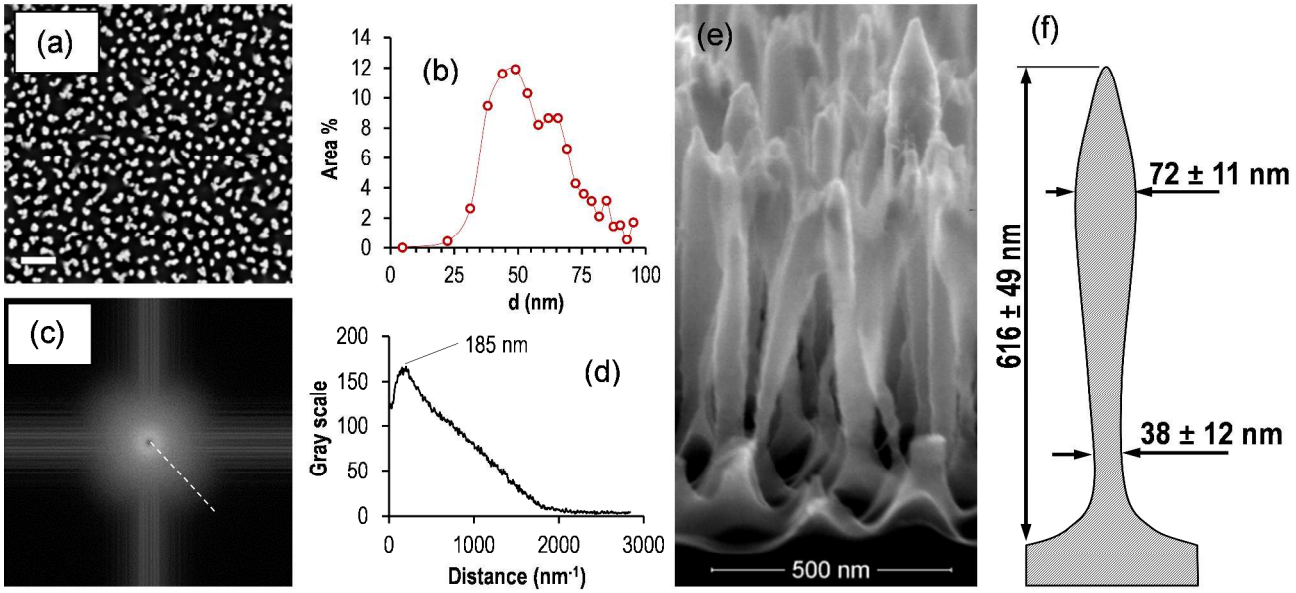

Fig. 1. Characterisation of the bSi nanopillar arrayed surfaces. (a) Top view SEM image of bSi (scale bar 500 nm), (b) area % distribution of the pillars quantified at widest cross-section, showing a maximum at 49 nm in area % at the widest pillar width, aggregation represented by the shoulder and tailing in the distribution extending to ~100 nm, (c) Fast Fourier 2D Transform of SEM image (a) yields an intense ring extended to four broad orthogonal lobes from this secondary structure, (d) radial grey scale intensity (0-255) profile showing the intense sharp ring in the centre peaks at a frequency distance of 185 nm, characteristic of the average distance between pillars with extended shoulders representing secondary pillar ordering, (e) side view of bSi nanopillars and (f) schematic representation showing dimensions calculated from average ± variance of 50 measurements of five SEM images.

3.2 Time-dependent interactions of erythrocytes with bSi surfaces

The time-dependent interaction of erythrocytes with the substrate surfaces was examined using SEM (Fig. 2 and Fig. S1) for periods up to 180 min, to establish their ultimate

stability. The surface cells on bSi that remained intact, and therefore maintained their biconcave discoid shape, were able to be clearly differentiated from their damaged and ruptured counterparts, where traces of the cell membrane remained on the uppermost layer of the nanopillars (Fig. 2a). Cell attachment on the bSi could be directly compared to that on the control surfaces: glass, gelatin-glass, and planar silicon wafer (Fig. S2), where cells that had adhered to the surface remained intact over this extended time period. The total number of cells that attached to the bSi surface increased with increasing incubation time and was found to be comparable to that on the planar Si wafer surface (Fig. 2b), indicating a system that is dominated by gravitational sedimentation, without the effects of the projected contact (tip) area. The maximum surface attachment density observed on the nanopillar array in this system was ~1.5 $\times 10^4$ cells mm^{-2}, where whole blood diluted to a haematocrit of 2% provides about 1×10^9 cells mL^{-1}. Once attached, the RBCs ruptured by the action of the bSi surface (Fig. 2c) where the proportion of ruptured cells to unruptured cells increased (Fig. 2c) to approximately 87% of the total number of cells that had adhered to the surface, after which time the surface appeared to be dominated by ruptured cells.

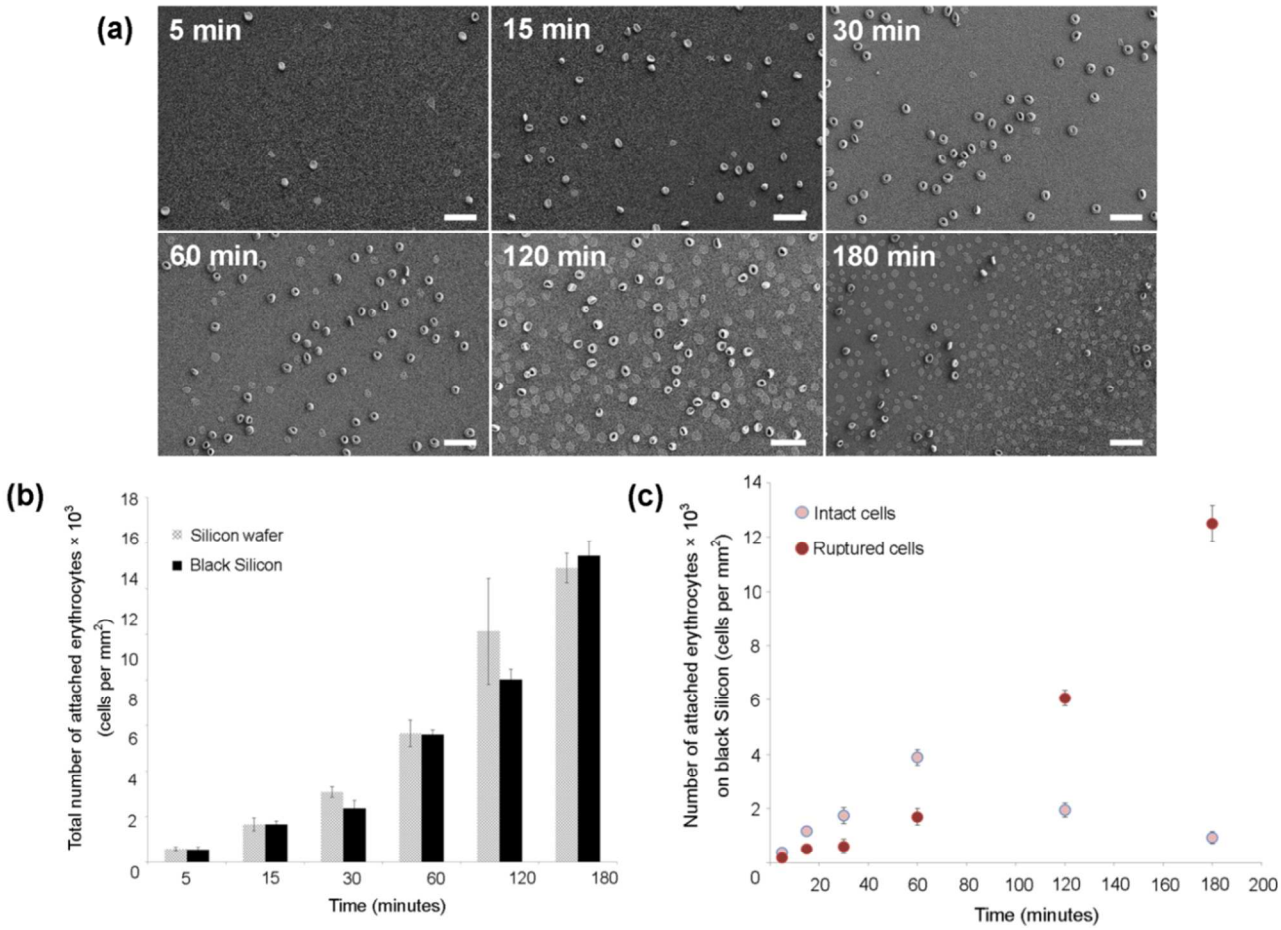

Fig. 2. Time dependent erythrocyte interactions with bSi nanopillar arrayed surfaces. (a) SEM images (top view) showing interaction of RBC with the bSi surface over three hours of contact. (b) comparative quantification of the dynamic attachment of RBC on bSi and commercial silicon wafers; data were plotted as an average of the total number of attached cells from 10 different areas in 3 independent experiments. (c) proportion of intact and ruptured RBC on bSi; RBC that maintained their biconcave shape on the surface were regarded as intact cells and the 'cell prints' of the damaged cells regarded as 'ruptured cells' (scale bar 20 μm).

3.3 Cell-rupture by nanopillar arrayed surfaces

Examination of the contact points of a single erythrocyte in contact with the nanopillars on the bSi surface on both the top and side view SEM images allowed the stages of cell deformation to be distinguished (Fig. 3a, b). On initial contact with the surface, the natural biconcave cell morphology was seen to be deformed, decreasing the cellular volume. The estimated reduction in cell contact area represents a linear strain ($\Delta l / l_0$) of approximately 18.6% compared to that existing prior to the loss of membrane integrity, engulfment and lysis. Confocal laser scanning microscopy (CLSM) confirmed that the erythrocytes were ruptured under liquid conditions, where the various stages of cell – surface interaction were clearly

evident (Fig. 3c). These images can be compared to the behaviour of the cells on the planar control surfaces, where no inactivation took place (Fig. S3). The fluorescently labelled cells appeared to be deformed, with the amount of fluorescence progressively fading as cell lysis occurred. Optical microscopy was used to record the real time attachment of RBCs on the bSi surface (Fig. S4). The time taken for the cells to be immobilised to their disappearance by rupture was found to be approximately 3 min for the cells observed within the field of view (Supporting Information, Video V1).

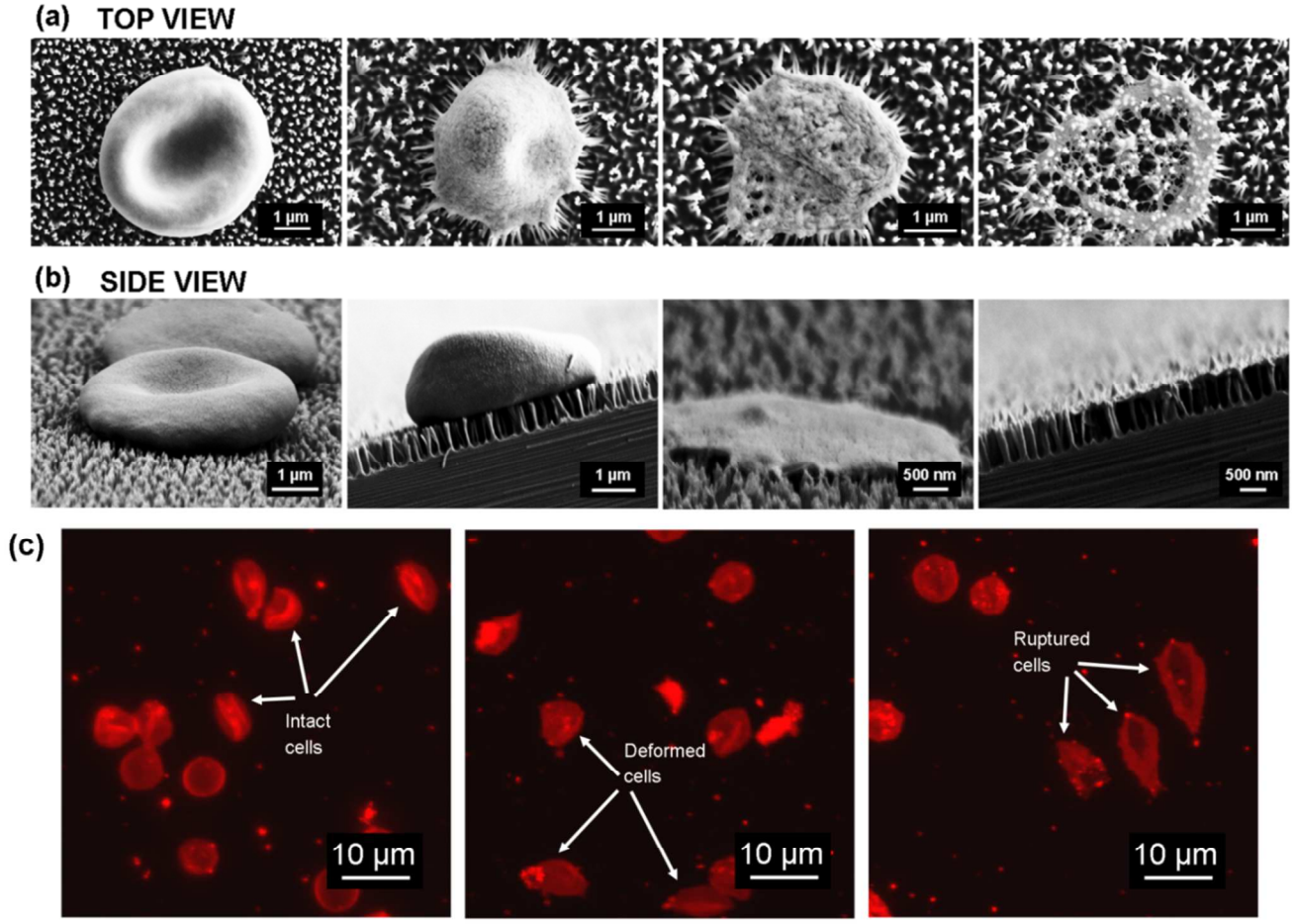

Fig. 3. The morphological alteration of erythrocytes interacting with nanopillar surfaces. SEM micrographs (a) top and (b) side view showing the step-by-step morphological changes taking place as a healthy, biconcave cell ruptures as a result of the action of the nanopillars. Segments of ruptured cell membrane can be seen which may be regarded as 'cell print'. (c) CLSM analysis confirmed the rupturing of RBC. Cells stained with 1,1'-dioctadecyl-3,3,3',3'-tetramethylindocarbocyanine perchlorate.

Nanopillars were observed to bend towards the erythrocytes, indicating a significant level of cell affinity for the surface (Fig. 3a). Studies of the interaction of a few mammalian cell types, such as embryonic stem cells[16, 30] and hippocampal neurons[31-33] with nanostructured surfaces highlighted that high aspect-ratio surface structures may lead to increased adhesion strength, decreased cell mobility and high cell retention. In these studies, no biocidal effect was reported, rather it was shown that these nanostructured surfaces were compatible with these cell types; the enhanced cell attachment was seen to improve communication with the cell interior, facilitating the delivery of biomolecules into cells or improving the extent of electrical signalling within neurons.

Raman spectroscopic analysis allowed a further insight into the impact of nanopillar contact with erythrocytes, also under liquid conditions (Fig. 4), where excitation at 532 nm provided the Raman resonance conditions for both the bSi and erythrocyte components.[34-36] The information provided in Fig. 4 allows further visualisation of the stages of erythrocyte attachment and disruption, when imaged between the integrated RBC Raman active range of 1100 to 3500 cm^{-1}. The transition from a normal biconcave discoid RBC (B) to a that of a

deformed cell morphology (C) is clearly seen in Raman shift image, where the corresponding spectra shows the on-set of a Raman peak at 2700 cm^{-1} for cell C undergoing cell rupture, which may be due to an enhanced nanopillar resonance but which is not present in the un-deformed cell (B).

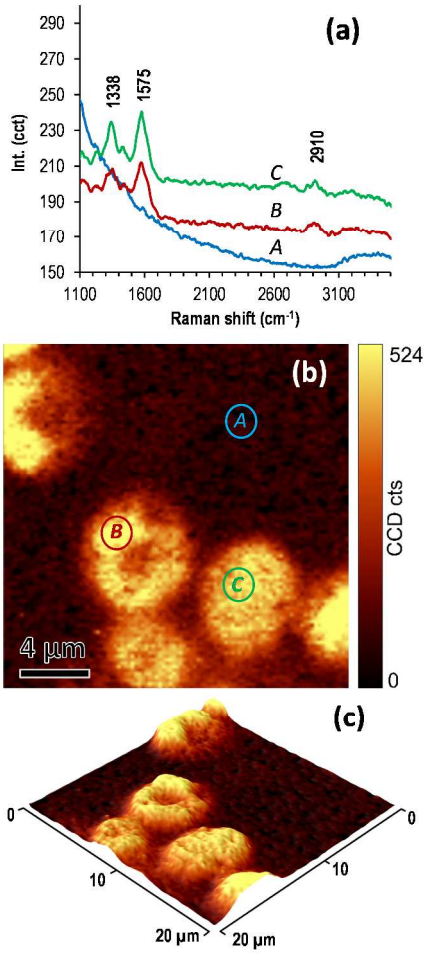

Fig. 4. Raman analysis of attached and ruptured erythrocytes on the bSi surfaces. (a) Spectra in the area of bSi and RBC (B,C) Raman activity from 1100 cm^{-1} to 3500 cm^{-1}, which provides discrimination from the bSi nanopillar resonance peak at 480 cm^{-1}. (b) (A) Raman spectrum in the RBC absent area, (B) RBC prior to disruption, and (C) ruptured RBC. Erythrocytes were incubated in the presence of bSi for 30 minutes in all experiments.

3.4 Erythrocyte membrane – nanopillar interactions

Well-established experimental and theoretical studies have drawn a correlation between the viscoelasticity of erythrocytes to the macromolecular arrangement of their membrane skeleton, which contains a spectrin-actin polygon network that reinforces the surface membrane.[37] This skeletal network allows erythrocytes to undergo significant extensional deformation whilst maintaining their structural integrity.[38] Thus, erythrocytes also possess a nanotopology that originates from their spectrin skeleton network. This network has a thickness of approximately 7.9 nm and is anchored to the phospholipid bilayer, which results in membrane spaces of approximately 162 nm × 65 nm as reported by Liu et al.[39, 40]. A reversible physical deformation of erythrocytes from their natural biconcave discoid can occur under relatively small force gradients of the order of 1 nN/µm in shear flow. The shear elastic modulus has been determined experimentally to be in the range 4-10 µN m^{-1} (micropipette technique) to ~2.5 µN m^{-1} (optical tweezers technique), while the area expansion modulus was found to be 300-500 mN m^{-1}.[23, 41] The schematic representation shown in Fig. 5 allows the interface between the microstructure of the erythrocyte lipid bilayer membrane (with its underlying and reinforcing spectrin–actin network situated on the inner cytoplasmic surface, having both junctional nodes anchoring transmembrane protein nodes[38]) and the bSi nanopillar surface, to be examined. A reconstruction of an AFM image of Liu et al.[40] of the cytoplasmic side of a lectin immobilised erythrocyte is also provided in Fig. 5, which has been processed to provide comparable image parameters to that of the nanopillar array given in Fig. 2. The area distribution of the nanopillars, quantified at a distance 20 nm from the pillar tip, is given in Fig. 5b. The data indicate an average diameter of approximately 12 nm, while the corresponding area distribution of the freestanding lipid bilayer within the network mesh size displayed an average distance distribution of approximately 52 nm. Hence, on average, 3 to 4 nanopillar contact points may interact with each unanchored lipid bilayer region on the erythrocyte, subjecting it to a deformational strain, both between the nanopillars and between the nanopillars and the spectrin anchored bilayer.

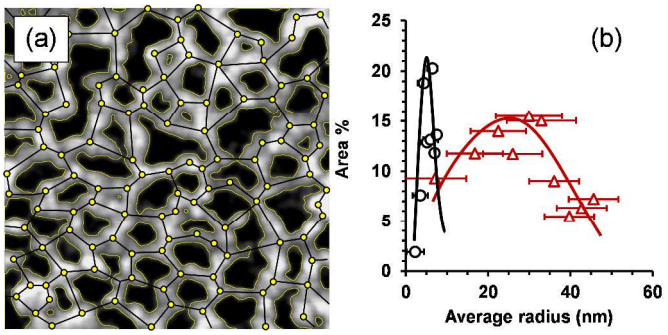

Fig. 5. Interfacial topology between bSi and erythrocyte membrane architecture. Fig. 5a gives the area distribution of the RBC cytoplasmic membrane surface determined by reconstructing the AFM image of immobilised RBC of Liu et al.[40] through image analysis consisting of: adjustment of bSi SEM (20 nm from nanopillar tip) and the RBC AFM image to comparable contrasts, colour thresholding, boundary delimination by variance transformation, backgrounding and summation of area distributions. The freestanding RBC lipid bilayer (black) represented approximately 50% of the geometrical area defined by typical junctional nodes, shown by the yellow points). Fig. 5b provides the average size distribution of the bSi nanopillars and the corresponding freestanding lipid bilayer areas between where it was anchored to the spectrin network of the RBCs.

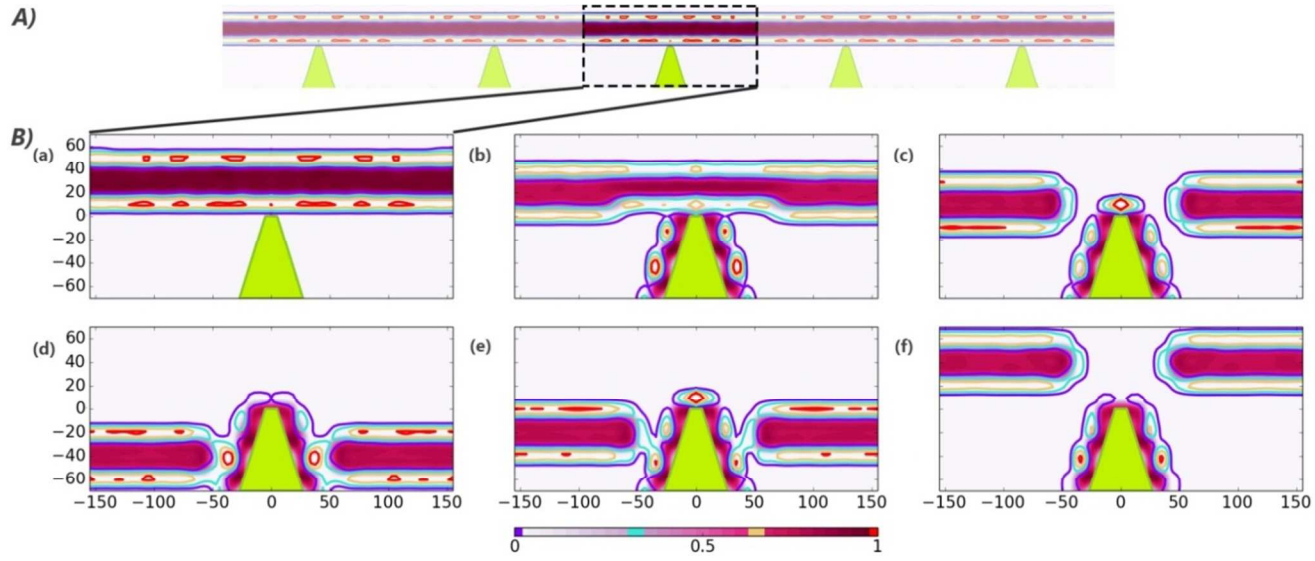

Fig. 6. Single Chain Mean Field density profile of a lipid bilayer in contact with regularly distributed nanopillars. (A) General view of the lipid bilayer and the tips of the pillars and the simulation box representing the mesh of the 3D periodic structure. The box size represents the spacing between nanopillar tips. (B) A sequence of solutions corresponding to relative positions of the bilayer with respect to the nanopillar. The distances are given in Angstrom, while the colours of the bilayer represent the volume fraction of tails and heads from 0 to 1 (below).

Within these unanchored lipid bilayer areas, the interaction between the nanopillar and the lipids has been modelled using a Single Chain Mean Field theory (SCMF) simulation, where the lipid is represented by two hydrophobic and one hydrophilic freely jointed spherical beads, connected by rigid bonds. The driving force for insertion and punching into the bilayer arises from an attraction between parts of the lipid to the hydrophilic bSi nanopillar.[28, 29, 42] Fig. 6 illustrates the changes that take place in the lipid bilayer density profile as a cell approaches a single nanopillar together, and its corresponding change in free energy. The difference in free energy between the unperturbed bilayer, the bilayer in contact with the nanopillar (deforming it but not piercing it), and the nanopillar piercing the bilayer to produce a pore in which it resides, is given in Fig. 7. Here, the initial reduction in free energy is seen on the approach of the attractive surfaces, most likely arising from loss of a solvation layer, followed by the deformation of the bilayer prior to the formation of a pore at approximately -20 nm, which is consistent with the parameters used in modelling the interfacial topologies given above. Insertion of the pillar, which leads to the rupture of the RBC, appears to reduce the free energy per nanopillar by about 200 kT over the 2 nm distance (Fig. 7), or by a change in force of about 400 pN. Subsequent nanopillar movement yields the hysteresis shown due to residual adhesion of lipid on the pillar similar to insertion seen with carbon nanotubes.[43]

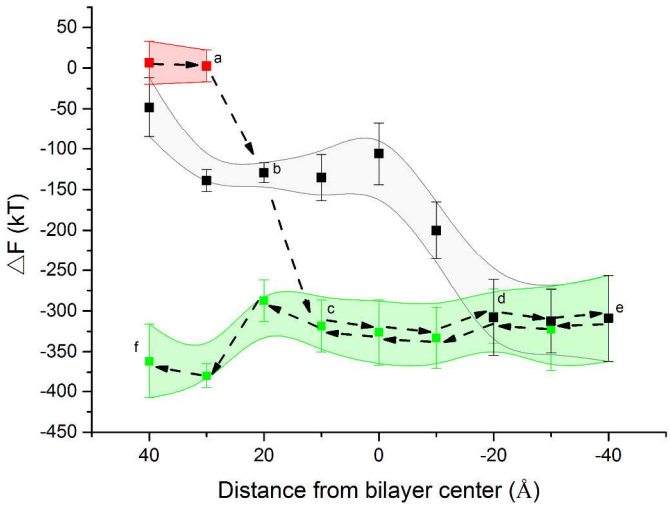

Fig. 7. Free energies driving nanopillar insertion. Free energy difference ΔF between unperturbed bilayer and the bilayer with inserted attractive cone as a function of the distance from bilayer center to the tip of the cone. Red stripe corresponds to the solution of unperturbed bilayer and a cone before the contact (reference state, zero energy); grey stripe corresponds to a cone touching the bilayer, but the bilayer is not pierced; green stripe corresponds to a cone induced a pore in the bilayer. Possible path (a)-(f) correspond to density profiles in Fig. 6B.

Conclusions

In this study, we demonstrated the spontaneous activity of a nanostructured surface in terms of the physical interaction that occurs between erythrocytes and the array of nanopillars present on the surface of bSi. This interaction is capable of

causing stress-induced cell deformation, rupture and lysis. The model topology was found to consist of an array of pointed bSi nanopillars, having a tip diameter of ~12 nm and pillar length of ~600 nm. SEM and real time optical microscopy indicated that erythrocyte rupture occurred via a process of initial surface adhesion, followed by the strain and deformation of intact cells by about 18% prior to their rupture, where the elapsed time between cell immobilisation to rupture was about 3 min. CSLM and integrated wavelength Raman imaging performed in the liquid state confirmed the existence of these stages of attachment and membrane disruption. Image analysis and reconstruction provided an insight into the convergence of the nanopillar topology and the RBC membrane microstructure, which showed that ~3 to 4 nanopillars on the surface of bSi were capable of interacting with the unanchored lipid bilayer region on the RBCs within the underlying spectrin-actin network. Finally, modelling the interaction between the nanopillars and the unanchored lipid bilayer in terms of a free energy driving force indicated that the spontaneous rupture of the lipid membrane occurred though direct piercing of the membrane by the nanopillars on the attractive bSi surface. The mechano-responsive bSi surface provides highly active, yet autogenous RBC lysis and therefore is an excellent prospect as an element in a front-end platform device in the evolving micro-fluidic platforms for cellular analyses.

Acknowledgements

We sincerely thank Debbie Lane for her assistance in collecting the rat blood from the Animal House, Monash University and Veselin Boshkovikj for his expertise in the formatting of images and video in this paper. We also acknowledge the RMIT Microscopy and Microanalysis Facility (RMMF).

Notes and references

[a]Department of Chemistry and Biotechnology, School of Science, Faculty of Science, Engineering and Technology, Swinburne University of Technology, PO BOX 218, Hawthorn, Victoria, 3122, Australia.
[b]Department d'Enginyeria Quimica, Universitat Rovira I Virgili, 26 Av. dels Paisos Catalans, 43007 Tarragona, Spain.
[c]Centre for Micro-Photonics, School of Science, Faculty of Science, Engineering and Technology, Swinburne University of Technology, PO BOX 218, Hawthorn, Victoria, 3122, Australia.
[d]Melbourne Centre for Nanofabrication, Australian National Fabrication Facility (ANFF), 151 Wellington Road, Clayton VIC 3168, Australia
151 Wellington Road, Clayton VIC 3168.
*Corresponding author
Elena P. Ivanova
Faculty of Science, Engineering and Technology, Swinburne University of Technology, email: eivanova@swin.edu.au.
† Electronic Supplementary Information (ESI) available. See DOI: 10.1039/b000000x/

1. J. Hu, S. Wang, L. Wang, F. Li, B. Pingguan-Murphy, T. J. Lu and F. Xu, *Biosensors and Bioelectronics*, 2014, **54**, 585-597.
2. K. B. Neeves, A. A. Onasoga and A. R. Wufsus, *Current Opinion in Hematology*, 2013, **20**, 417-423.
3. S. Dhanekar and S. Jain, *Biosensors and Bioelectronics*, 2013, **41**, 54-64.
4. H. W. Hou, A. A. S. Bhagat, W. C. Lee, S. Huang, J. Han and C. T. Lim, *Micromachines*, 2011, **2**, 319-343.
5. A. A. S. Bhagat, H. Bow, H. W. Hou, S. J. Tan, J. Han and C. T. Lim, *Medical and Biological Engineering and Computing*, 2010, **48**, 999-1014.
6. A. A. S. Bhagat, H. W. Hou, L. D. Li, C. T. Lim and J. Han, *Lab on a Chip - Miniaturisation for Chemistry and Biology*, 2011, **11**, 1870-1878.
7. R. Fan, O. Vermesh, A. Srivastava, B. K. H. Yen, L. Qin, H. Ahmad, G. A. Kwong, C. C. Liu, J. Gould, L. Hood and J. R. Heath, *Nature Biotechnology*, 2008, **26**, 1373-1378.
8. C. T. Lim and A. Li, *Theoretical and Applied Mechanics Letters*, 2011, **1**, 014000.
9. H. W. Hou, W. C. Lee, M. C. Leong, S. Sonam, S. R. K. Vedula and C. T. Lim, *Cellular and Molecular Bioengineering*, 2011, **4**, 591-602.
10. J. Kim, M. Johnson, P. Hill and B. K. Gale, *Integrative Biology*, 2009, **1**, 574-586.
11. D. W. Lee and Y. H. Cho, *Sensors and Actuators, B: Chemical*, 2007, **124**, 84-89.
12. Y. Huang, E. L. Mather, J. L. Bell and M. Madou, *Fresenius' Journal of Analytical Chemistry*, 2002, **372**, 49-65.
13. E. A. Schilling, A. E. Kamholz and P. Yager, *Analytical Chemistry*, 2002, **74**, 1798-1804.
14. V. Anandan, Y. L. Rao and G. Zhang, *Int. J. Nanomed.*, 2006, **1**, 73-79.
15. M. A. Bucaro, Y. Vasquez, B. D. Hatton and J. Aizenberg, *ACS Nano*, 2012, **6**, 6222-6230.
16. K. S. Brammer, C. Choi, C. J. Frandsen, S. Oh and S. Jin, *Acta Biomater.*, 2011, **7**, 683-690.
17. E. P. Ivanova, J. Hasan, H. K. Webb, V. K. Truong, G. S. Watson, J. A. Watson, V. A. Baulin, S. Pogodin, J. Y. Wang, M. J. Tobin, C. Löbbe and R. J. Crawford, *Small*, 2012, **8**, 2489-2494.
18. J. Hasan, H. K. Webb, V. K. Truong, S. Pogodin, V. A. Baulin, G. S. Watson, J. A. Watson, R. J. Crawford and E. P. Ivanova, *Appl. Microbiol. Biotechnol.*, 2013, **97**, 9257-9262.
19. E. P. Ivanova, J. Hasan, H. K. Webb, G. Gervinskas, S. Juodkazis, V. K. Truong, A. H. F. Wu, R. N. Lamb, V. A. Baulin, G. S. Watson, J. A. Watson, D. E. Mainwaring and R. J. Crawford, *Nat. Commun.*, 2013, **4**, 2838.
20. D. R. Gossett, W. M. Weaver, A. J. MacH, S. C. Hur, H. T. K. Tse, W. Lee, H. Amini and D. Di Carlo, *Analytical and Bioanalytical Chemistry*, 2010, **397**, 3249-3267.
21. M. I. Tiirikainen, *Cytometry*, 1995, **20**, 341-348.
22. V. L. Lew, T. Tiffert and H. Ginsburg, *Blood*, 2003, **101**, 4189-4194.
23. G. Lenormand, S. Hénon, A. Richert, J. Siméon and F. Gallet, *Biophys. J.*, 2001, **81**, 43-56.
24. V. K. Truong, R. Lapovok, Y. S. Estrin, S. Rundell, J. Y. Wang, C. J. Fluke, R. J. Crawford and E. P. Ivanova, *Biomaterials*, 2010, **31**, 3674-3683.

25. H. K. Webb, V. Boshkovikj, C. J. Fluke, V. K. Truong, J. Hasan, V. A. Baulin, R. Lapovok, Y. Estrin, R. J. Crawford and E. P. Ivanova, *Biofouling*, 2013, **29**, 163-170.
26. J. L. Unthank, J. M. Lash, J. C. Nixon, R. A. Sidner and H. G. Bohlen, *Microvasc. Res.*, 1993, **45**, 193-210.
27. F. Lassailly, E. Griessinger and D. Bonnet, *Blood*, 2010, **115**, 5347-5354.
28. S. Pogodin and V. A. Baulin, *Soft Matter*, 2010, **6**, 2216-2226.
29. A. Ben-Shaul, I. Szleifer and W. M. Gelbart, *J. Chem. Phys.*, 1985, **83**, 3597-3611.
30. W. Kim, J. K. Ng, M. E. Kunitake, B. R. Conklin and P. Yang, *J. Am. Chem. Soc.*, 2007, **129**, 7228-7229.
31. W. Hällström, T. Mårtensson, C. Prinz, P. Gustavsson, L. Montelius, L. Samuelson and M. Kanje, *Nano Letters*, 2007, **7**, 2960-2965.
32. J. T. Robinson, M. Jorgolli, A. K. Shalek, M. H. Yoon, R. S. Gertner and H. Park, *Nat. Nanotechnol.*, 2012, **7**, 180-184.
33. C. Xie, L. Hanson, W. Xie, Z. Lin, B. Cui and Y. Cui, *Nano Letters*, 2010, **10**, 4020-4024.
34. N. A. Brazhe, S. Abdali, A. R. Brazhe, O. G. Luneva, N. Y. Bryzgalova, E. Y. Parshina, O. V. Sosnovtseva and G. V. Maksimov, *Biophys. J.*, 2009, **97**, 3206-3214.
35. N. A. Brazhe, E. Y. Parshina, V. V. Khabatova, A. A. Semenova, A. R. Brazhe, A. I. Yusipovich, A. S. Sarycheva, A. A. Churin, E. A. Goodilin, G. V. Maksimov and O. V. Sosnovtseva, *J. Raman Spectrosc.*, 2013, **44**, 686-694.
36. E. Y. Parshina, A. S. Sarycheva, A. I. Yusipovich, N. A. Brazhe, E. A. Goodilin and G. V. Maksimov, *Laser Phys. Lett.*, 2013, **10**.
37. K. i. Tsubota and S. Wada, *Int. J. Mech. Sci.*, 2010, **52**, 356-364.
38. J. C. Hansen, R. Skalak, S. Chien and A. Hoger, *Biophys. J.*, 1997, **72**, 2369-2381.
39. A. H. Swihart, J. M. Mikrut, J. B. Ketterson and R. C. Macdonald, *J. Microsc.*, 2001, **204**, 212-225.
40. F. Liu, J. Burgess, H. Mizukami and A. Ostafin, *Cell Biochem. Biophys.*, 2003, **38**, 251-270.
41. S. Hénon, G. Lenormand, A. Richert and F. Gallet, *Biophys. J.*, 1999, **76**, 1145-1151.
42. S. Pogodin, J. Hasan, V. A. Baulin, H. K. Webb, V. K. Truong, T. H. P. Nguyen, V. Boshkovikj, C. J. Fluke, G. S. Watson, J. A. Watson, R. J. Crawford and E. P. Ivanova, *Biophys. J.*, 2013, **104**, 835-840.
43. E. J. Wallace and M. S. P. Sansom, *Nano Letters*, 2008, **8**, 2751-2756.